energies

MDPI

Article

Effect of the Inclusion of Photovoltaic Solar Panels in the Autonomy of UAV Time of Flight

Joana Engana Carmo [1], João Paulo Neto Torres [1,2,3], Gonçalo Cruz [4] and Ricardo A. Marques Lameirinhas [1,2,*]

[1] Department of Electrical and Computer Engineering, Instituto Superior Técnico, 1049-001 Lisbon, Portugal; joana.carmo@tecnico.ulisboa.pt (J.E.C.); joaotorres@tecnico.ulisboa.pt (J.P.N.T.)
[2] Instituto de Telecomunicações, 1049-001 Lisbon, Portugal
[3] Academia Militar, Av. Conde Castro Guimarães, 2720-113 Amadora, Portugal
[4] Portuguese Air Force Research Center, 2715-311 Sintra, Portugal; gccruz@academiafa.edu.pt
* Correspondence: ricardo.lameirinhas@tecnico.ulisboa.pt

Abstract: Photovoltaic technology and unmanned aerial vehicles are both alluring areas with a lot of potential to explore. Consequently, they have an ability to adapt and progress when faced with new challenges, hence their wide range of applications. An auspicious combination between the two is born from the Unmanned Aerial Vehicles' (UAVs) inability to to overcome some of its problems, namely the autonomy one. This article springs from the need to vanquish the problem, finding a more permanent solution. Its aim consists in the installation of solar photovoltaic panels in the structure of a UAV, with the objective of studying being its influence on the vehicle's time of flight. To accomplish this, a theoretical study will be made, encompassing all the potential variables together with its influence. In order to verify the credibility of these claims, a prototype, based on the original aerial vehicle structure form and material, is constructed, using a finite element tool. Later, the prototype is used to evaluate possible harsh circumambient air to structure interactions, modeled by the fluid motion describer Navier–Stokes equations. For a smooth approach involving lighter computational power, a RANS model is used to asses the equations. Based on its results the chosen solar technology credibility is evaluated. A simulation of solar cells will also be carried out, accepting as input previously studied parameters which will modify its performance. Bearing in mind the produced results, it is concluded that the solar panels can only significantly augment the time of flight in very specific conditions.

Keywords: autonomy; optics; photovoltaic technology; time of flight; solar cell; unmanned aerial vehicles

Citation: Engana Carmo, J.; Neto Torres, J.P.; Cruz, G.; Marques Lameirinhas, R.A. Effect of the Inclusion of Photovoltaic Solar Panels in the Autonomy of UAV Time of Flight. *Energies* **2021**, *14*, 876. https://doi.org/10.3390/en14040876

Received: 31 December 2020
Accepted: 5 February 2021
Published: 8 February 2021

1. Introduction

The main drive behind aircraft development was always human beings' desire for a fast and safe transportation of people and cargo [1]. Around the time of the First World War, 1916, the first Unmanned Aerial Vehicles (UAVs) appeared, with the primary application being the military one, solving gradually, as the air-crafting was enhanced, the problems of the D3-Dull, Dirty and Dangerous-missions. UAVs started blooming for other applications at the birth of the 21st century and its use is still growing at current times.

UAVs are still raw in terms of potential for they carry many issues which currently have no ultimate solution and that can affect negatively their performances, making them unreliable in some cases. The research object of this article is centered around the improved autonomy of UAVs. Currently, there are many efforts trying to progress in order to achieve a relatively general solution to make these vehicles reliable in terms of energy for a long term usage, guaranteeing that key aspects of the UAV's operation are not compromised. Up-to-date, the most appealing solution consists in the inclusion of solar cells in the UAV structure, enabling the collection of solar energy to increase the time of flight [2].

Solar panels were created by Charles Fritts in mid 1880s and were considered by the inventor a way to revolutionize the energy production and the related pollution [3]. From its birth to current times, solar technology keeps evolving and adapting to the consumer needs, taking into particular consideration the resonating factor: its efficiency [4–19]. Although its importance is unquestionable, the UAVs have, as aforementioned, aspects that cannot be discredited, being a shape that cannot be altered and a weight that can fluctuate fairly from the original value. Therefore, a combination of the UAV and photovoltaic technologies can be considered challenging, for the conditions must be fulfilled.

The present research aims to solve the autonomy problem by the augmentation of the time of flight. This will be achieved including thin film photovoltaic solar panels wrapped around the UAV structure, so that solar energy can be used to charge the vehicle's batteries. Ideally, the resulting electrical energy from the implemented panels will be able to increase considerably the time of flight, taking a further step into turning the photovoltaic technology a viable, and perhaps definite, solution to the improved autonomy problem.

2. Project Contextualization and Theoretical Background

2.1. Unmanned Aerial Vehicle Contextualization

As it was aforementioned, the purpose of this article is the study of the effect the implementation of solar photovoltaic panels in the aircraft structure will have in the autonomy of UAV time of flight. The considered aerial vehicle has achieved a maximum continuous flight duration of 40 min in the electrical propulsion configuration, availing itself of 3.7 V nominal voltage Li-Po batteries, due to its good energy density, light weight and flexibility. Ten battery cells are used, in a series configuration, to feed the propulsion system and only three are appointed to power the remnant systems.

In the case study, it is of utmost importance to take into consideration the altitude at which the machine flies, thereby, taking into account some of the variables that affect the performance of the solar cells. By definition, altitude is a distance measured between a reference and an object or point. In this work, two different references are regarded: ground and sea level. The first grants that the UAV's observation conditions are optimized when keeping a distance to it from 200 m to 800 m, preferably 400 m and the second enables the assessment of the aerodynamic and propulsion questions. According to the sea level, the maximum altitude at which the UAV flies is 2000 m.

The case study is based in a UAV that has a range of 20 km over land and 5 km over sea. Usually the aerial vehicle in question departs from the CIAFA which is located at Pêro Pinheiro, Lisbon district, reason why in this article it will be considered, for simplification, the starting point. When climbing the aerial vehicle has an Angle of Attack (AOA) of 30° and for the cruise flight a much minor angle of 3°.

The energy steamed in the solar panels is expected to be able to enhance the aerial vehicles time of flight by its storing in the batteries, narrowing the effects of the propulsion and other systems power consumption [4–19]. In order to do that, appropriate solar cells need to be chosen. However, before any considerations can be made, it is of utmost importance to know the UAV's available area for implementation. Two surfaces will be considered: the wings, each with a height of 278 mm and a width of 1009 mm and the booms, each composed by two parallel faces with a height of 45 mm and a a width of 553 mm.

2.2. Photovoltaic Technology Selection

Nowadays, photovoltaic cells are divided into three generations: wafer based or first generation, whose method of fabrication consists in creating slices, or wafers, of semiconductor material; thin-film or second generation, focused in producing flexible and weightless cells, with the disadvantage of lower efficiency; and third generation or emerging photovoltaics, which endeavors to achieve first generation efficiency with second generation thin-film technique without the use of toxic and limited materials [4–19].

When choosing a solar technology it is of utmost importance to guarantee its compatibility with the surface which will support the cells. The objective of this article is extremely sensitive to additional weight and due to its reduced dimensions needs the highest efficiency possible, reason why both the first and second generations were excluded. As a result of its high efficiency and accessible non-toxic material, second generation Flexible Thin Crystalline Silicon solar cells, were chosen as the preferred to coat the UAV [4–19]. Typically this type of cells have a thickness between 20 µm and 50 µm, length from 50 mm to 100 mm, width with range from 0.5 mm to 1.5 mm and are most commonly made of mono-crystalline silicon [20].

2.3. Solar Cell Performance Fluctuation

2.3.1. Influence of the Wind

In order to recreate a wind flow the most similar possible to reality, it is considered a turbulent wind flow, which is characterized by its irregular and chaotic fluctuations in the particles' movement, with rapid variations of pressure and velocity.

Thinking of a flow in a pipe, the flow average velocity profile increases drastically when slightly away from the wall and after remains approximately constant due to the mixing between different layers of flow, introduced by the turbulence. A no-slip condition exists right at the pipe wall, ensuring that the flow velocity there is always zero. This condition also makes high shear stresses near the wall, resulting in the creation of a very thin boundary layer. The boundary or turbulent boundary layer has two different layers: the buffer layer and the laminar or viscous sub-layer. Closer to the wall layer (viscous sub-layer) the viscous forces—frictional forces due to fluid viscosity—dominate and the flow is laminar. The above layer is the buffer, where both viscous and turbulent effects are significant, resulting in a mix of both flows. The upper limit of this layer is the turbulent boundary, that denotes the end of both the buffer and the turbulent layers. Above it, the turbulent effects dominate and by consequence the flow is turbulent. The turbulent flow has whirls regions called eddies. They are part of an energy cascade where large eddies—which have high energy—feed the creation of small eddies that will hereafter dissipate into heat due to viscosity. Lewis Fry Richardson said "big whirls have little whirls that feed on their velocity and little whirls have lesser whirls and so on to viscosity".

Navier-Stokes are a set of differential equations which express the motions of fluids by describing how its characterization parameters - like the density, temperature, pressure and velocity—are related. They have a wide range of practical uses, for example the modeling water currents, the weather, air flow, which all insert itselves on the modeling flow field. The set of Equations (1) counts with the fluid density ρ, the fluid velocity $\mathbf{u}$, the fluid pressure p and the fluid dynamic viscosity μ.

$$\begin{cases} \rho\left(\frac{\partial \mathbf{u}}{\partial t} + \mathbf{u}\cdot\nabla\mathbf{u}\right) = \\ = -\nabla p + \nabla\cdot\left[\mu\left(\nabla\mathbf{u} + (\nabla\mathbf{u})^T - \frac{2}{3}(\nabla\cdot\mathbf{u})\mathbf{I}\right)\right] + \mathbf{F} \\ \frac{\partial \rho}{\partial t} + \nabla\cdot(\rho\mathbf{u}) = 0 \\ \rho = \rho(p,T) \end{cases} \quad (1)$$

Navier-Stokes first equation represents the conservation of moment, composed by the inertial forces $\rho\left(\frac{\partial \mathbf{u}}{\partial t} + \mathbf{u}\cdot\nabla\mathbf{u}\right)$, the pressure forces $-\nabla p$, the viscous forces $\nabla\cdot\left[\mu\left(\nabla\mathbf{u} + (\nabla\mathbf{u})^T - \frac{2}{3}(\nabla\cdot\mathbf{u})\mathbf{I}\right)\right]$ and lastly, the external forces applied to the fluid $\mathbf{F}$.

Wind flow around the UAV structure will be here studied with resource to a Turbulent Flow module. This module aims to solve the Navier-Stokes equations by modeling the fluid domain around the airflow, as a mesh of discrete elements. The study will use a stationary analysis, which signifies the annulment of the inertial forces first term $\frac{\partial \mathbf{u}}{\partial t}$. To

simplify, an incompressible flow approximation is also considered, the continuity equation-Navier-Stokes second equation $\frac{\partial \rho}{\partial t} + \nabla \cdot (\rho \mathbf{u}) = 0$ yields

$$\nabla \cdot \mathbf{u} = 0 \Rightarrow -\frac{2}{3}(\nabla \cdot \mathbf{u}) = 0. \tag{2}$$

The equations will be evaluated with resource to the computational assessment technique RANS, a time averaged method which which doesn't resolve eddies explicitly, choosing to instead model its effect using the concept of turbulent viscosity. RANS is not an explicit method and therefore is less computationally expensive, being that the primary reason for its use in this work. After applying the RANS method (time averaging) to the described Navier-Stokes, further simplifications are made, obtaining the Equation (3) for the conservation of moment. It is of utmost importance to accentuate the appearance of the term $\rho\overline{\mathbf{u}'\mathbf{u}'}$, named Reynolds stress, which results from the time-dependent fluctuations that are not solved by the time-averaging method.

$$\rho(\overline{\mathbf{u}} \cdot \nabla \overline{\mathbf{u}}) = -\nabla \overline{p} + \mu \Delta \overline{\mathbf{u}} - \nabla \cdot (\rho \overline{\mathbf{u}'\mathbf{u}'}) + \mathbf{F} \tag{3}$$

By the use of $k - \epsilon$ turbulence model, the Reynolds stress is modeled into $\mu_t(\nabla \overline{\mathbf{u}} + (\nabla \overline{\mathbf{u}})^T) - \frac{2}{3}\rho k \mathbf{I}$, where μ_t is the turbulent viscosity and k the turbulent kinetic energy. The final RANS system of Equations (4) is achieved.

$$\begin{cases} \rho(\overline{\mathbf{u}} \cdot \nabla \overline{\mathbf{u}}) = -\nabla \overline{p} + (\mu + \mu_t)\Delta \overline{\mathbf{u}} - \frac{2}{3}\rho k \mathbf{I} + \mathbf{F} \\ \nabla \cdot \overline{\mathbf{u}} = 0 \\ \rho = \rho(p, T) \end{cases} \tag{4}$$

Wall functions are adopted to resolve the thin boundary layer near the wall, preventing the use of a very fine mesh. Essentially they provide an offset so that the mesh does not need to go near the wall, moreover, being the solution there straightforward, a relationship is used to characterize the flow.

A rise of the height causes an increase in the velocity of wind until the superior limit of the Atmospheric Boundary Layer (ABL) is reached. To model the variation of wind speed with height, inside the boundary layer, the logarithmic profile law can be used, giving the the horizontal wind speed for the desired height. Equation (5) describes the logarithmic profile law, where v_h is the velocity at the desired height Z_h, v_{an} is the velocity at the anemometer height Z_{an} and the term Z_0, the surface roughness length, also comes into view. This parameter is expressed in meters and characterizes the hardness and stability of the surrounding land.

$$v_h = v_{an} \times \left| \frac{\ln(Z_h/z_0)}{\ln(Z_{an}/z_0)} \right| \tag{5}$$

2.3.2. Influence of the Cell Temperature

The solar cell surface's temperature is an important parameter to the photovoltaic (PV) conversion—due to the semiconductor's sensitiveness to heat—whereas its rise will significantly decrease the cell's output power. A study made by John K. Kaldellis, Marina Kapsali and Kosmas A. Kavadias analyzed the effect the velocity of wind can have in the cell's temperature, concluding that almost a diminish of 1 °C in the cell temperature can be seen, per augment of 1 m s^{-1} of wind's velocity, turning the wind a significant factor to the cell's temperature measurement.

To find out how wind speed affects the cell temperature a study was consulted, where eight different criterion—which all "parameterize the physical relation between cell temperature, incoming irradiance and relevant meteorological parameters"—are tested to different cells. By analysis of its values it can be established that the better approach for monocrystalline solar cells is the Skoplaki 2 [21].

Skoplaki 2 is an advanced model which derives from the Standard approach by the inclusion of wind data. In the Standard approach or NOCT-Sandard-formula, the most commonly used for cell temperature T_c calculation, the wind cooling effect is not included. It is determined according to Equation (6) and it is based on Nominal Operating Cell Temperature (NOCT) conditions, where T_{NOCT} defined as the temperature reached by open circuited cells (different for each cell technology) measured with ambient temperature $T_{a,NOCT}$ of 20 °C, irradiance I_{NOCT} of 800 W m^{-2} and wind speed of 1 m s^{-1}. T_a is the ambient temperature and I is the in-plane irradiance.

$$T_c = T_a + \frac{I}{I_{NOCT}} \cdot (T_{NOCT} - T_{a,NOCT}) \tag{6}$$

Equation (7) describes the Skoplaki 2 model. It is composed by the Standard approach (first part of the equation) together with wind data and Standard Test Conditions (STC) resulting parameters. STC are the industry standard conditions under which solar panels are tested. There is guaranteed an irradiance of 1000 W m^{-2}, ambient temperature T_{STC} of 25 °C and an air mass of 1.5, from which parameters like the efficiency η_{STC} and the temperature coefficient of maximal power β_{STC} are determined.

$$T_c = \frac{T_a + \frac{I}{I_{NOCT}} \cdot (T_{NOCT} - T_{a,NOCT}) \cdot \frac{h_{w,NOCT}}{h_w(v)} \cdot \left[1 - \frac{\eta_{STC}}{\tau \cdot \alpha}(1 + \beta_{STC} T_{STC})\right]}{1 - \frac{\beta_{STC}\eta_{STC}}{\tau \cdot \alpha} \cdot \frac{I}{I_{NOCT}} \cdot \frac{h_{w,NOCT}}{h_w(v)} \cdot (T_{NOCT} - T_{a,NOCT})} \tag{7}$$

his model also considers the transmittance of the cover system τ, the absorption coefficient of the cells α—the value for $\tau \cdot \alpha$ will be assumed as 0.9—and the wind convection coefficient h_w, defined in Skoplaki 2 by the parameterization (8), where v_h is the velocity of the wind at desired height. Lastly, $h_{w,NOCT}$ is the wind convection coefficient for wind speed under NOCT conditions, which, similarly to the last described variable relies on Equation (8) with v_h equal to 1 m s^{-1}.

$$h_w = 5.7 + 2.8 v_h \tag{8}$$

2.3.3. Influence of the Pressure

Air pressure, also called barometric pressure, is the pressure enforced by the air weight on a point or place of the Earth's atmosphere. It is intuitive to think that a high-pressure area is associated with a large atmospheric mass above its location, on the contrary, low-pressure areas have a smaller atmospheric mass overhead its location. To summarise, whereas altitude rises the atmospheric pressure declines, being the reason for that the decrease of the overlying atmospheric mass [22].

A method to calculate the air pressure, P_hs is provided in Equation (9). It considers the pressure at sea level P_0, the desired height h_s—to which it is subtracted concerning the height at the bottom of the atmospheric layer h_0—along with its respective temperature T_{hs} and uses the following constants: universal gas constant, R, with value 8.3143 N m mol^{-1} K^{-1}, gravitational acceleration constant, g equal to 9.807 m s^{-2} and molar mass of Earth's air, M of 0.028 96 kg mol^{-1}.

$$P_{hs} = P_0 \cdot \exp\left(-\frac{Mg}{RT_{hs}} \cdot (h_s - h_0)\right) \tag{9}$$

Although some components of the wind flow can have a positive effect on the UAV flight, the majority of the others will only create pressure on the surface of the airplane. The magnitude of the incident pressure will vary with the force applied by the turbulent wind flow. The latter will depend on its kinetic energy, which in turn depends on the velocity. When the kinetic energy of the flow increases, so does the pressure.

For the case study the reaction of the solar cells after being subjected to pressure is an important variable. When in contact with the photovoltaic cells, pressure can cause

damage, such as fissures, having the possibility of rendering the whole module useless. The pressure a cell can take before damage occurs will depend on its material and shape. This influence will be latter studied with simulations, alongside the wind flow, to make sure it is possible to apply photovoltaic technology on the UAV without the possibility of breaking.

2.3.4. Influence of the Irradiance

Solar irradiance is the radiant energy the sun produces normally accounted as Global Horizontal Irradiance (GHI), which is the total radiation received on an horizontal plane on Earth, composed by the sum of direct irradiance and diffuse irradiance [4–19].

Irradiance suffers an augment as altitude increases. The influencing factors for that variation are first and foremost optical path and ground albedo. It is almost instinctive to affirm that when reducing the geometrical path length from origin to destination an enlargement of the "receiving signal" will occur, in essence, the optical path can be viewed as a function of the altitude, for its diminish will imply a consequent decrease on the attenuation of the radiation by the atmosphere. Likewise, clouds, aerosols and water vapors—predominantly located in the lower atmosphere—also play a part in the radiation's weakening. Lastly, the ground albedo or reflection coefficient will have an impact on irradiance diffuse component (proportional to the albedo) which will be higher as proximity to ground increases, thereupon reflecting negatively on GHI [23].

There are many researches concerning the best approach to determine the variation of the received GHI with altitude. For this study, while the fluctuation of the parameter was theoretically investigated and its importance explained and recognised, none of the existing models is intended to be used for its values, for the desired height, will be considered at subsequent simulations.

3. Parameter Physical Influence

With the object of this article being a UAV there is a need to simulate the in study variables, like the wind flow and the pressure, around its structure, so that its effect on the solar cells can be accounted. Furthermore, bearing that in mind, a 3D model of the to be used aerial vehicle was constructed, with resource to the Fimite Element tool's Geometry.

To simplify the work, the UAV was divided in parts, grouping the geometrically similar ones, with the idea to join component to component until the airplane was completely formed. The wings were chosen as the base to start drawing. They were made first in a 2D yz plane, with parametric curves, and after extruded (in the x axis) to the desired width of 2.508 m. Next, the booms and the tail were drawn, in 3D from the start, as they are made of simple geometries like prisms and straight-lined polygons. The tail is composed by the rudders, elevator, vertical and horizontal stabilizers. For the "body" or fuselage, a separate geometry component was created guaranteeing that its overlap with the wings would not interfere with the drawing. A further division in upper, middle and lower fuselage was needed to represent it, by cause of the structure complexity. The upper and lower segments were made with resource to 3D ellipsoids, cut by the middle on both the yz and xy planes. A composition of ellipsoids was also used to form the middle segment—which is not hollow in the intern part—all cut on the yz plane. An ellipsoid was also used to form the nose. Joining all the components presented so far, resulted in the final aerial vehicle of Figure 1

The physical unmanned vehicle is made of a composite material which includes fiber glass, carbon fiber and epoxy resin. Its properties make it resistant and light in order to ensure the structure withstands the mechanical stresses that it is subjected to, and at the same time that its weight does not over burden the motor subsequently increasing the energy consumption. Ideally, the material chosen for the simulation should be the same the physical UAV is made of, however, the most similar one is a composite with only fiber glass and epoxy resin, forgoing some of the strength the carbon fiber endows the composite with.

As aforementioned, wind flow around the UAV structure and consequent pressure will be studied with resource to the Turbulent Flow module. The simulation's input geometry is a wind tunnel with dimensions of 3.5 m width, 5.5 m depth and 22.5 m height with the previously designed UAV inside. For the height, the ideal would be a wind tunnel with 2000 m, so that the unmanned vehicle could be shifted to the desired altitude to simulate. However, a geometry that substantial, mainly in comparison with the vehicle's dimensions, would mean an excessively above normal computational power. Instead, variables like the ambient pressure, temperature and wind velocity at the open boundary are used as an input to replicate the desired altitude conditions.

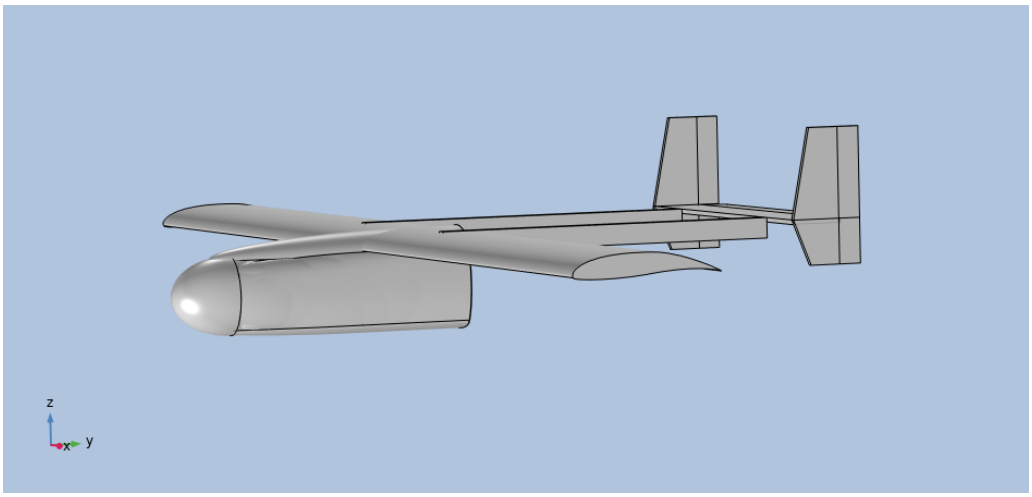

Figure 1. Unmanned Arial Vehicle (UAV) drawn prototype.

First thing to contemplate is the altitude in question, only after that the other variables can be determined. Concerning the wind velocity inserted at the open boundary (wind tunnel top), its value was calculated using the previously exposed logarithmic profile law (Equation (5)). A surface roughness length z_0 of 3.0 m was used, emulating a terrain hardness corresponding to city centers and tall buildings, to the actuation zone being Lisbon district. The wind average velocities were gathered at Lisbon district in 2019, arriving to the maximum and minimum values 5.14 m s^{-1} and 3.22 m s^{-1}. Temperature was the next input variable to resolve. On that account, the average higher and lower values at Lisbon district were researched, reaching values of 29 °C and 8 °C, respectively. For its variation with height a drop of 2 °C per 300 m, relatively to the ambient temperature at ground-level, will be considered. On the part of the reference air pressure, the previously exposed Equation (9) is the base for its calculation. While most of its parameters are constants, the temperature T_{hs} and desired height h_s will vary according to the simulated conditions. For the remaining parameter, the height at the bottom of the atmospheric layer h_0, it was defined as 0 m. The change in the ground altitude at the radius of actuation is not constant but is never significantly higher, relatively to the considered, meaning that, per se it will not interfere drastically with the results.

Starting with the highest altitude—2000 m at UAV level and 2010 m at the top—the maximum values of temperature (29 °C at ground level) and average wind speed (5.14 m s^{-1} at ground level), the values of 48.25 m s^{-1}, 288.82 K (15.67 °C) and 79,981.01 Pa were calculated for the wind speed at the top boundary, reference temperature and pressure, respectively. An AOA of 30° is considered, simulating the climbing.

On Figure 2 the resulting wind flow is illustrated, being characterized by velocity magnitude—differentiated by colors whose legend can be seen at the right border—orientation and direction. As it was expected, due to the way the velocity varies with height, the maximum is located at the top boundary, with equal value to the inserted, and its value decreases with altitude, reaching a minimum value between 40 m s^{-1} and 35 m s^{-1}. Near the UAV a sudden drop on the velocity occurs on the account of the "shielding" the vehicle

structure makes to the area immediately near it. Wind flow orientation and direction are represented by the black arrow lines at the outer boundaries of the tunnel. Its length is proportional to the magnitude.

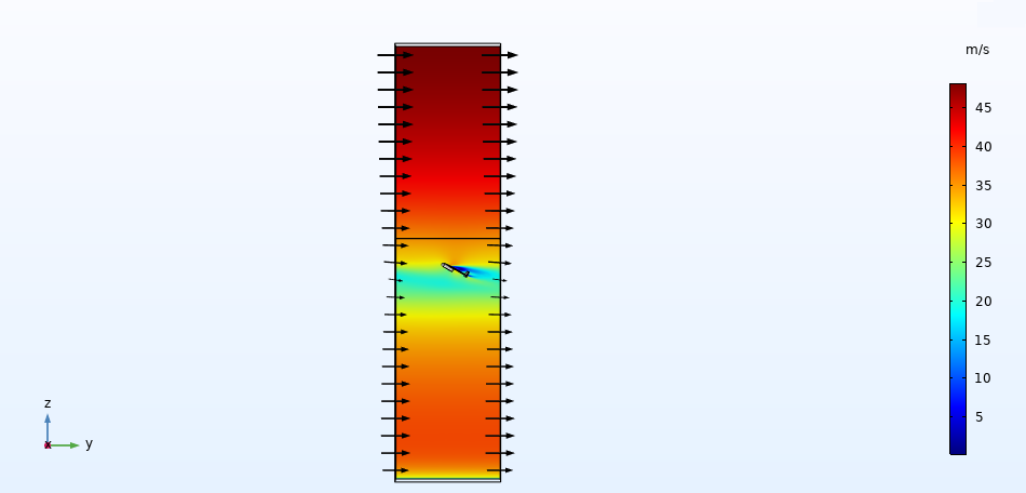

Figure 2. Maximum wind flow in m s^{-1} at 2000 m of altitude and 30° Angle of Attack (AOA).

A difference in the flow velocity magnitude "passing through" the different aerial vehicle's parts is also seen, denoting that they are not all affected equally. The lowest velocity is clearly behind the structure, justified by the "shelter", the most robust part of the vehicle (fuselage plus nose) creates against the flow passage. Thinking about the aerial vehicle motion when climbing, and crossing it with the presented information, it is expected the nose, the lower fuselage—due to the path the flow takes when confronted with the nose—and the wing's leading edge to be the surfaces that "suffer" the most, sustaining the wind flow. However, it is important to refer that this study is two dimensional, as such, the flow that focuses on some surfaces, like the wings, cannot be seen in detail. Nevertheless, it can still be noticed the lower velocity in the upper wings contrasting, with a velocity higher by almost 25 m s^{-1} at the bottom wing.

Both bottom and lateral views were chosen—illustrated in Figures 3 and 4, respectively—to assess the pressure study, which, like the wind flow one is differentiated by colors whose legend is present at the right border. It is important to reinforce that a reference pressure for the air surrounding the vehicle is provided, therefore, all the displayed values are relative to it, being the reference treated as a "zero" for the referential.

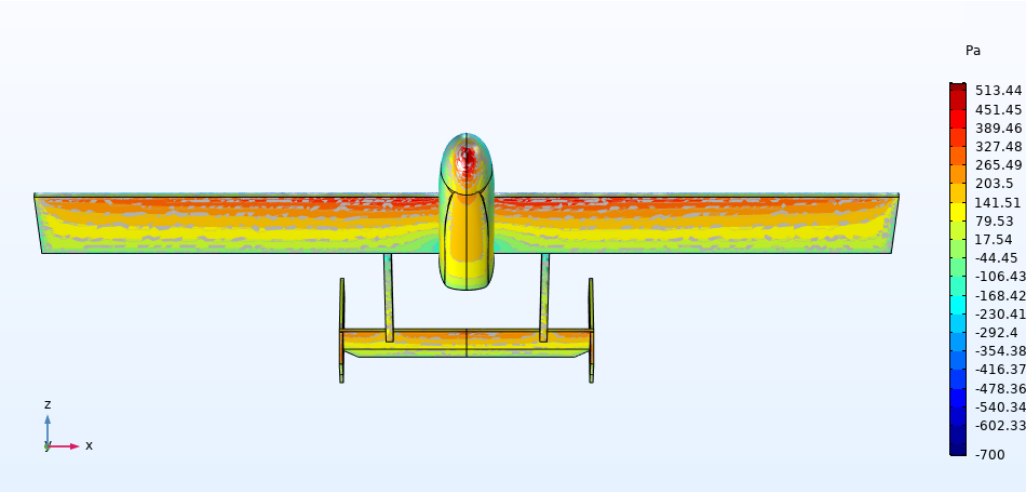

Figure 3. Bottom UAV focused view of maximum pressure in Pa at 2000 m of altitude and 30° AOA.

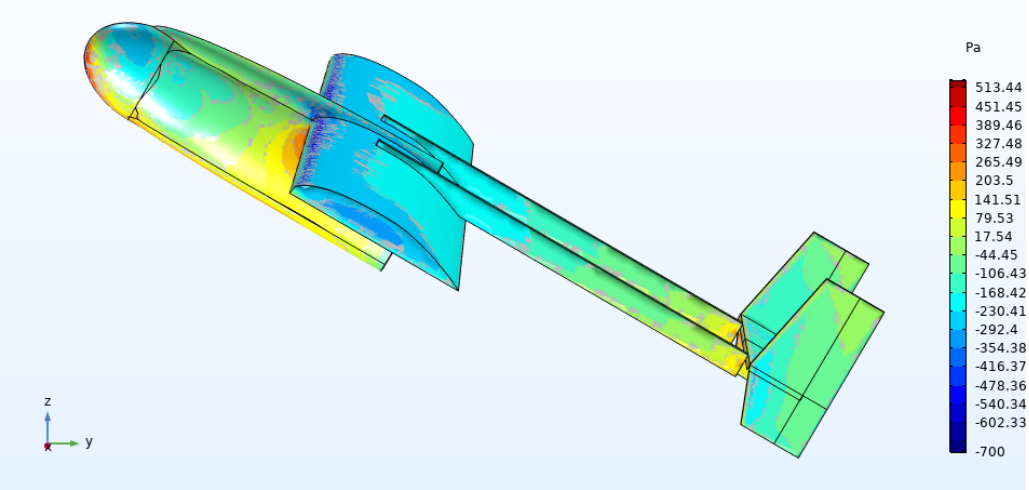

Figure 4. Lateral and top UAV focused view of maximum pressure in Pa at 2000 m of altitude and 30° AOA.

Being directly related with the air flow, it was expected a high pressure on the nose, lower fuselage, and down wing which is verified by the figures, where the highest pressure is located on the nose. Thinking about the UAV motion when climbing, the nose directly faces the flow, which will escape both by the top and bottom fuselage. The part that escapes to the top will mostly ascend and combine with the flow that is essentially not influenced by the airplane, thus never exerting its force on the UAV upper fuselage. On the contrary, the flow that escapes downwards exerts pressure in the lower part of the vehicle—by trying to rise—together with the flow that directly hits it, due to its frontal position in the movement.

Most like the nose, the airfoil lower part takes directly the flow. An undeniable contrast both in the pressure and surrounding velocity in between the upper and lower wing, is seen. This difference is highly responsible for the lift force. When hitting the down wing, the air is confronted with the wing inclined path that will push the air below it downwards. In turn, it will apply a high force on the wing surface to follow the forced path. Its pressure on the wing will reduce as the distance to the attack border increases, as more of the air will flow upwards, attracted by the low pressure area created by the higher wind speed above the vehicle. For the air that initially flows up, it will be sucked into the higher velocity-lower pressure area above, together with the air product of the down flow.

For a different perspective, cruise flight will be considered, with a 3° angle of attack, maintaining all the other conditions—pressure, temperature, altitude and wind speed. In Figure 5, the wind flow magnitude, orientation and direction are shown. Comparing with the simulations for the climbing, a clear difference is seen both at the velocity drop and the flow orientation and direction, in the vehicle surrounding space. While for the previous simulations the wind flow magnitude had considerable variations near the unmanned vehicle—from nearly 35 m s^{-1} to 5 m s^{-1}—the current one has more attenuated ones—from 40 m s^{-1} to 30 m s^{-1}. With the only changed variable being the angle, it is clear that the velocities own their values to the lack of "shielding" the UAV provides.

Again, a bottom and lateral views were used to evaluate the pressure in the unmanned vehicle structure, as illustrated in Figures 6 and 7, respectively. Comparing with the previous pressure values, the differences begin to show at the maximum and minimum values, which augmented, in modulus, about 100 Pa. With the drastic change in the wind flow magnitude around the vehicle, consequent alterations had to occur in the surface pressure distribution. Not minding the angle adjustment, a high pressure for the nose can be seen, as the surface will always face the flow "head on".

Identical to the nose, the leading edge of the wings directly faces the flow, suffering a high pressure for this reason. This edge will provoke a separation, as after impact, the air will both flow up and down the wing, not on equal measures. The air that flows down will

experience the same as previously described with a 30° angle, with the difference being the lesser inclination of the wing, that consequently will result in a minor force exerted by the air in the surface as it will be able to escape and ascend easily to the low pressure area.

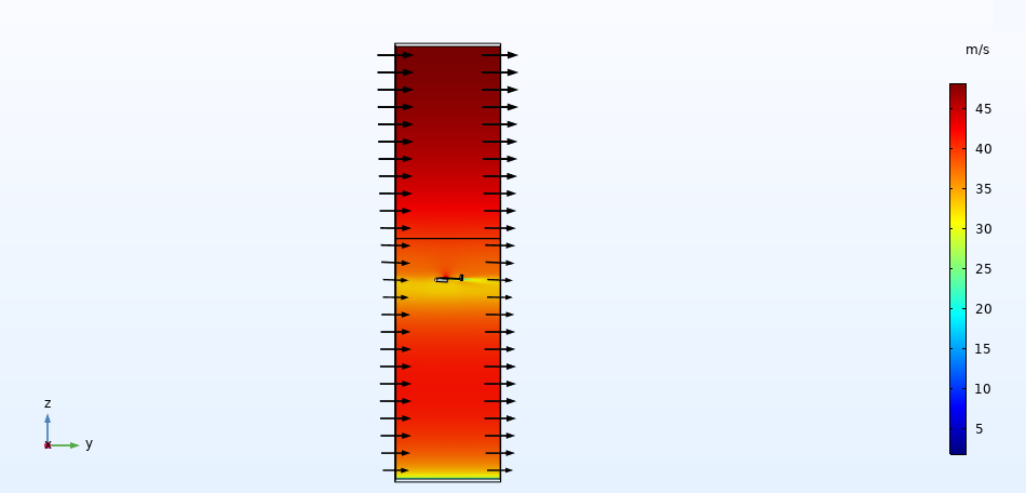

Figure 5. Maximum wind flow in m s^{-1} at 2000 m of altitude and 3° AOA.

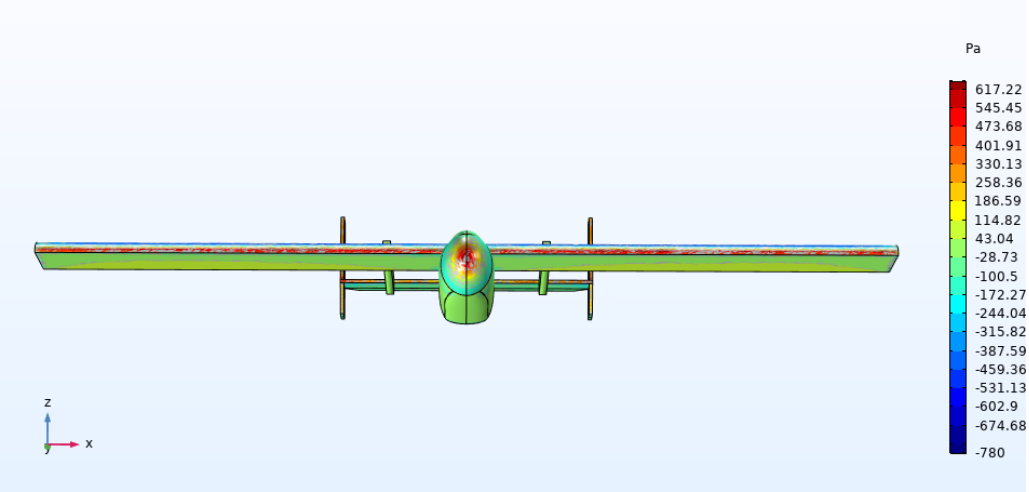

Figure 6. Bottom UAV focused view of maximum pressure in Pa at 2000 m of altitude and 3° AOA.

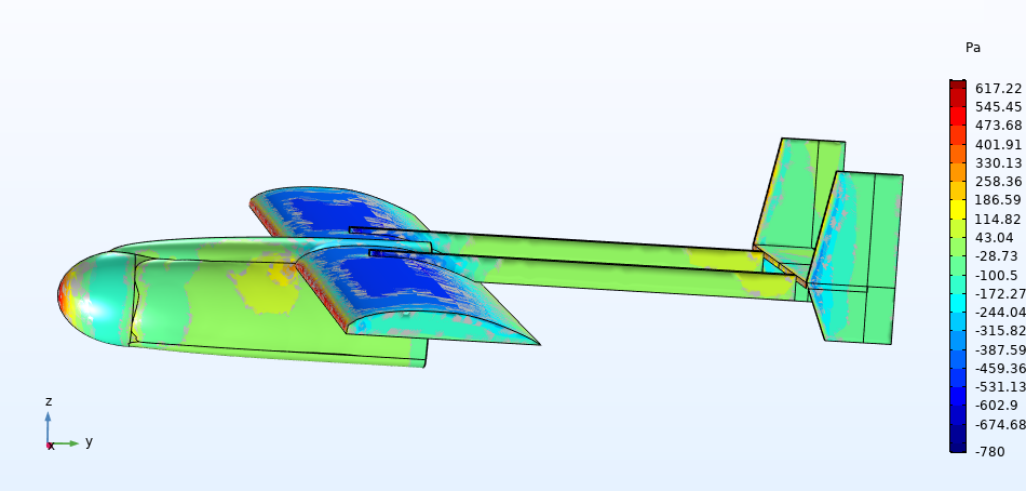

Figure 7. Lateral and top UAV focused view of maximum pressure in Pa at 2000 m of altitude and 3° AOA.

From the presented results some general conclusions can be taken. It can be said that the wind may affect the vehicle surface directly, when hitting the UAV, or indirectly, by the influence of the structure surrounding velocity. When in direct contact with the surface, a higher wind flow magnitude will induce a greater pressure in it. For the surrounding flow, that doesn't come into contact with the aerial vehicle, a higher velocity of the fluid means a lower pressure (by Bernoulli's principle) and vice-versa, thus, affecting the air flow, which tends to be attracted to lower pressure areas.

Comparing the information from the simulations the importance of the angle of attack is underlined. To guarantee the existence of the lift force —that holds the vehicle in the air—the angle of attack needs to be greater than zero, so that when confronted with the down wing surface, its bent path pushes the air downwards, which in turn will create the pressure responsible for the lift. The pressure is proportional to the angle of attack. For the vehicle to decrease altitude, a reduction of the lift force is required. This motions are made by decreasing the angle of attack and deflecting the elevators down. Nevertheless the pressure created at the top of the wings will not be much higher than the simulated, as summed to the weight it would highly unbalance the vehicle, being this the reason this motions were not viewed important for the case study, thus never considered.

As aforementioned, the purpose of these simulations consists in the evaluation of the influence of the wind flow and pressure on the UAV structure and consequently on the to be implemented panels. The upper limit of force the to be used flexible silicon cells can take without permanent damage (tensile yield strength) is about 0.7 GPa [20]. Comparing the previous results for the pressure concentrated on the wings and booms, the maximums are attained at 30° and 3° AOA, respectively. For the wings, as it can be seen in Figure 4, two different pressure values cover the wing surface, being the higher at the rear with value 79 750.6 Pa. Figure 7 booms, count with an almost constant value of pressure on its extensions, that slightly augments at the end near the tail, where a value of 80 024.05 Pa is displayed. Since none of this values are close to limit, it can be concluded that the wind flow and its ensuing pressure do not pose a threat to the solar cells integrity, thus validating the possibility for its implementation.

4. Photovoltaic Modules

4.1. Application Description

In order to appraise the to be included panels operation, considering the theoretically studied parameters, an application available on the Finite Element tool, that illustrates the operation at an user-specified location of a Si solar cell, will be used. It is highly dependant on user specified parameters, such as the altitude, location and cell's attributes, to characterize the cell performance, making it a good fitting to the case study. To handle the different types of inputs, the application combines two different modules, being them Ray Optics and Semiconductor.

For the concerning Ray Optics module, the Geometrical Optics interface is used to model, for a predefined position, the received irradiance through the day, at a specific date. It is based on the ray tracing algorithm that simulates the path of light, starting from the receiver object until the source. This module does not consider the scattering of the radiation by atmosphere particles and molecules, therefore, the direct radiation received by the solar cell from sunlight is the total radiation. The model measures the intensity of the directly incident radiation as a function of the following parameters: altitude above sea level, air mass and angle of incidence and reference irradiance. The reference irradiance is the only constant and will be here adapted to the average yearly value at Pêro Pinheiro, being it about 4400 $W\,m^{-2}$.

Semiconductor's module is used to compute the cell characteristics based on the Gauss law. To better define the conditions several interfaces are adopted, which resort to input design parameters provided by the user, naming the cell temperature, the shunt and series resistances and the azimuth and tilt angles. The used geometric model is a 1D PN junction with the anode and cathode modeled as thin ohmic contacts deposited on

the emitter and base side, correspondingly. To model the solar cell the Semiconductor module will interact with the Ray Optics, in order to obtain the spectral irradiance, which will be subsequently used to determine the generation rate. In its turn, the generation rate depends on the absorption coefficient and the photon generation rate. Counterbalancing the complexity of the equations, some valid assumptions are made: the spectral irradiance is approximated through sun's blackbody spectrum at temperature 5777 K and the anode is assumed as having the reflectance equal to one due to a perfect antireflecting coating.

With the objective of extracting the solar cell characteristics, namely the maximum power point—constituted by the voltage at maximum power V_{mp} and the current at maximum power I_{mp}—the short circuit current I_{sc} and the open circuit voltage V_{oc}, the application will generate the cell parameter correspondent I-V and P-V curves. The efficiency η will be calculated, with resource to Equation (10), where FF corresponds to the fill factor, given by the expression in Equation (11) and P_{in} is the incident power, defined by $P_{in} = H_0 A$, being A the solar cell area.

$$\eta = \frac{I_{sc} Voc FF}{P_{in}} \tag{10}$$

$$FF = \frac{I_{mp} V_{mp}}{I_{sc} V_{oc}} \tag{11}$$

4.2. Solar Cell Simulations

Starting to define the sunlight properties for the Ray Optics Computations, there was a need to specify both the zone coordinates, the date and the altitude. For the coordinates the Pêro Pinheiro zone is considered, with value (38.861077, −9.320995). To the date, the winter and summer solstice of 2019 were used, as they contrast with the shortest and longest light hours. Finally, for the altitudes, bearing in mind the variation of the irradiation and wind velocity with it, the maximum (2000 m) and the minimum (200 m) will be taken into account.

To characterize the cell properties, the cell temperature, the shunt and series resistances and the azimuth and tilt angles were detailed. The cell temperature will be calculated with resource to Equation (7), where the non-constant values, like T_a and $h_{w,NOCT}$ will depend on the considered altitude, thus, will be further specified on the respective simulation. For the solar cell series and shunt resistances, good commercial values are 1000 $\Omega\,cm^2$ for the first and 0.5 $\Omega\,cm^2$, which, according to the cell area of 25 mm^2, will have the final values of 4000 Ω and 2 Ω.

Commonly, the azimuth is defined as the angle between the object and the meridian of the location, however, the program was made with the south hemisphere in mind, intrinsically making the azimuth referent to north and defined as positive to east. A detailed measurement of the cell azimuth angle is not feasible, for the UAV can fly in every direction, therefore, the simulations will be made with the maximum and minimum values. For the last property, particularly the tilt angle, the cruise flight angles are chosen, due to the reduced time the vehicle spends climbing. As a result, the angle of 3° is used for the wings and 90° for the booms. The azimuth and tilt angles are the only parameters that exhibit a difference, amidst the booms' and wings' solar cells. For the booms there is even a further distinction in the azimuth angle between sides of the same boom, being this the reason for separate simulations for wings and booms. The maximization and minimization of these parameters is made for the wings, seeing that for its position and extension they will produce higher output energy.

Opening with the simulations for the maximum values, the date 21 June 2019 was used, corresponding to summer solstice, the day with more light hours of the year, together with an altitude of 2000 m, being based in a cell temperature of 21.89 °C (295.04 K), obtained with $T_a = 15.67$ °C, predetermined $I = 1043\,W\,m^{-2}$ and wind velocity of 48.22 $m\,s^{-1}$. The UAV has an AOA of 3° which corresponds to a tilt of −3°, as such, its favored direction of flight to minimize the incident angle will be north, which equals an azimuth of 0°. These

values originated Figure 8 where the direct irradiance received by the cell on the wings' surface can be seen. For every sunlight incident simulation the values are only displayed since the sun rises until the sun sets. If a value is not present for the sunlight incident angle, the direct irradiance is programmed to be assumed as zero.

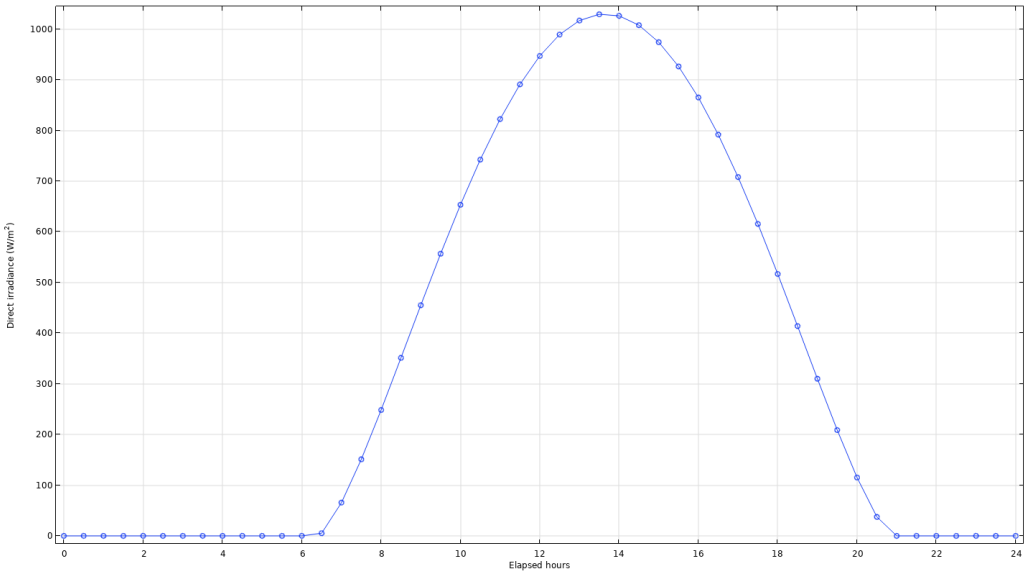

Figure 8. Direct Irradiance (W m^{-2}) received by the cell at 2019's summer solstice, referent to the wings.

The UAV in context has two booms with a right side and a left side each. To simulate this situation, different azimuth angles were used for the faces with distinct faces, always with a tilt angle of 90°. When the vehicle is flying north, each boom has a side facing east and another facing west. To emulate the east faces, an azimuth angle of 90° is used, generating the direct irradiance in Figure 9. By facing east with a 90° tilt, it is natural for the cell to only receive light in the morning and early afternoon hours and even then due to its angles the irradiance values will be lower than the wings' ones.

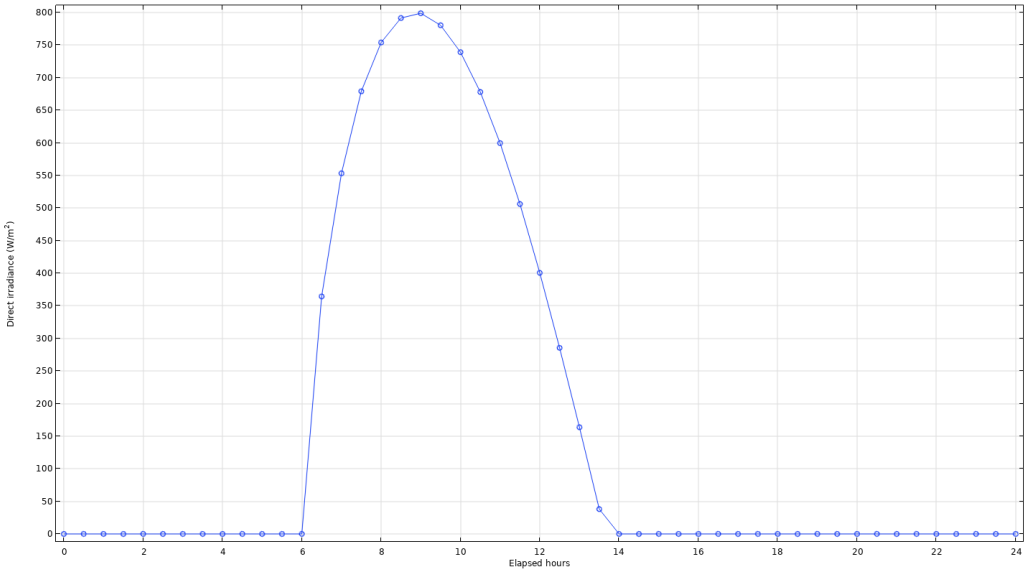

Figure 9. Direct Irradiance (W m^{-2}) received by the cell at 2019's summer solstice, referent to the boom's east sides.

A rotation of 180° from the east faces azimuth angle is used to generate the west ones, which count with an azimuth of 270°. The corresponding graphic for the direct irradiance can be observed in Figure 10. Due to its azimuth and tilt angles' values, the west side booms only start to receive light in the afternoon, almost right when it ends for its counterparts.

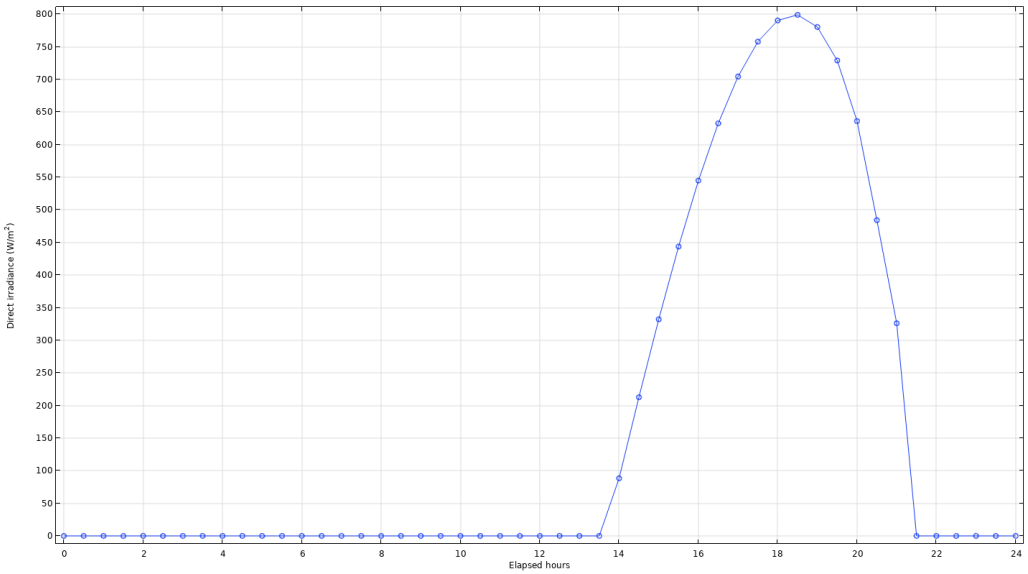

Figure 10. Direct Irradiance (W m^{-2}) received by the cell at 2019's summer solstice, referent to the boom's west sides.

The last simulations are made with the objective to produce the minimum values possible, so that a complete range of the output energy is made. For the date, the winter solstice, 22 December 2019, the shortest day of the year, was chosen, together with an altitude of 200 m. The cell temperature, was calculated, having the value of 21.1 °C, obtained with $T_a = 6.67$ °C, predetermined $I = 388$ W m^{-2} and a wind velocity of 19.51 m s^{-1}.

For the minimum values, it was considered a UAV flying in south direction (azimuth of 180°) with a tilt angle of −3°. These values were behind the creation of Figure 11 where the irradiance received by wings' surface cell can be seen. Comparing to the wing's last results, a clear reduction of both the active hours and received irradiance can be seen, which will have major implications on the output energy the cell can produce.

There is no need to distinguish the maximum and minimum value simulations in terms of booms' angles. So, bearing that in mind, the east faces will still have an azimuth of 90° and the same value for the tilt angle, generating the direct irradiance graphic illustrated in Figure 12.

Considering the already explained 270° azimuth angle, together with the −3° tilt angle, the graphics for the direct irradiance can be subsequently observed in Figure 13, for the west side of the booms. Again, with the 180° discrepancy from the east faces, the sunlight will only focus on these cells by early afternoon, more specifically, at 2 pm.

All these previously illustrated and described graphics concerned the external variables that, although they may affect the energy output the cell will have, by means of the reduction of the irradiance, they do not condition or influence the cell internal operation and subsequently its efficiency. Of the constant parameters heretofore characterized only the series resistance, the shunt resistance and the cell temperature have an impact in the cell efficiency.

Varying the load resistance R_{load}, the application obtained the I-V and P-V curves illustrated in Figures 14 and 15, from where the maximum power point, I_{sc} and V_{oc} were extracted. The efficiency was determined with the referred parameters and the provided solar cell area of 25 mm (50 mm long × 0.5 mm narrow), obtaining a value of 17.92 %, based on Equation (10).

The previously computed I-V and P-V curves were determined for one isolated solar cell, with 25 mm^2 (50 mm $\times$ 0.5 mm) of area. In order to ascertain the total output power, the number of cells that fit in the UAV considered structures need to be calculated. Each wing has a total length of 1009 mm and a width of 278 mm—excluding the aileron—where, a line of 20 cells can be made at length and column 556 at width, composing a total of 11,120 cells, that conceive a singular wing panel. For one face of the boom, the length is 503 mm and the width 45 mm, therefore, a line of 11 cells and a column of 90 cells can be made, forming a panel of 990 cells.

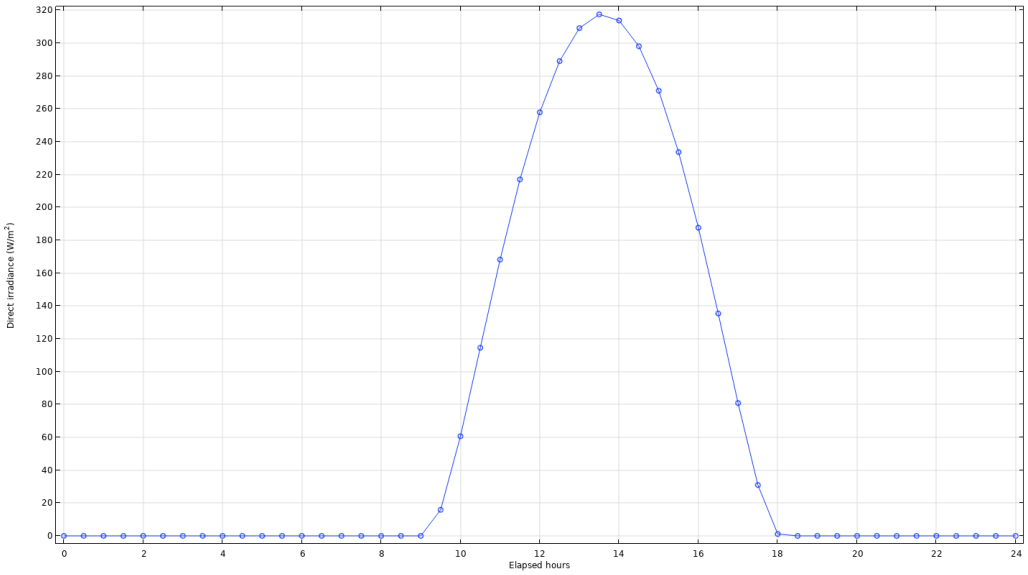

Figure 11. Direct Irradiance (W m^{-2}) received by the cell at 2019's winter solstice, referent to the wings.

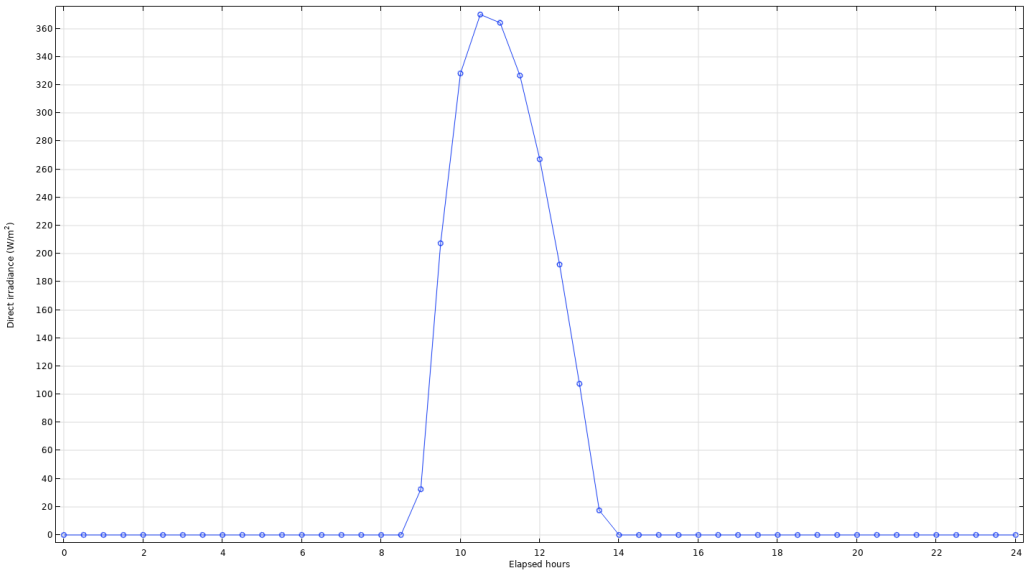

Figure 12. Direct Irradiance (W m^{-2}) received by the cell at 2019's winter solstice, referent to the boom's east sides.

With the number of cells of each panel calculated, the connections are shaped, thus, permitting the settlement of the voltage and current values. It was decided with the number of cells in mind, to associate the column cells in parallel, with the link between different columns being a series connection, both for the wings and boom's faces. These connections will show its effects in the current and voltage, as expected, with the parallel

bonds augmenting the current in each point proportionally to the number of lines and the series bonds having the same effect on the voltage, which will increase proportionally to the number of columns. Being constituted by series and parallel connections of the already presented silicon solar cell, the panels have merely an increase in the voltages and currents, nonetheless counting with the same characteristics. On that manner, the efficiency maintains itself the same as the single photovoltaic cell, cutting the need to make any further calculations.

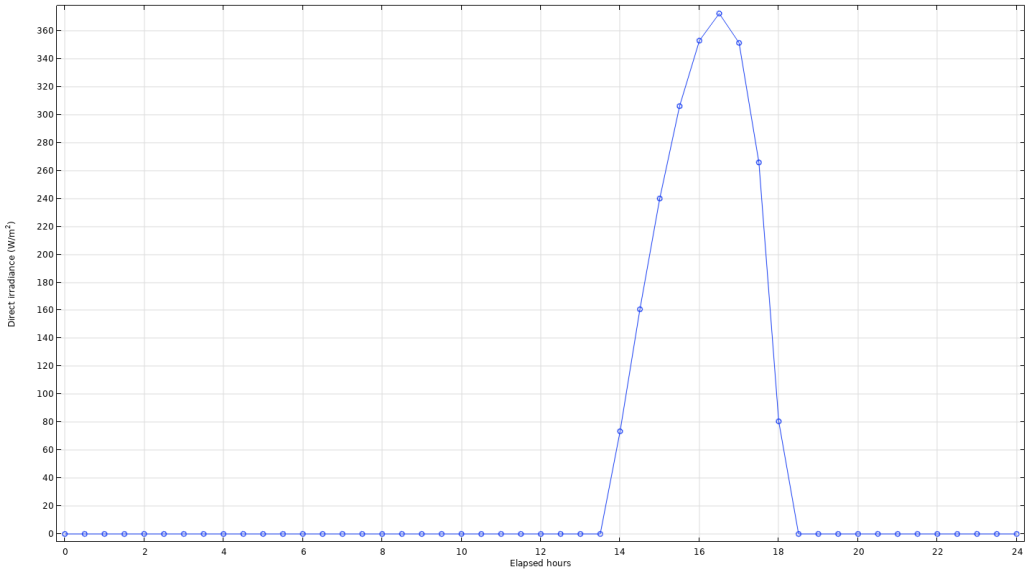

Figure 13. Direct Irradiance (W m^{-2}) received by the cell at 2019's winter solstice, referent to the boom's west sides.

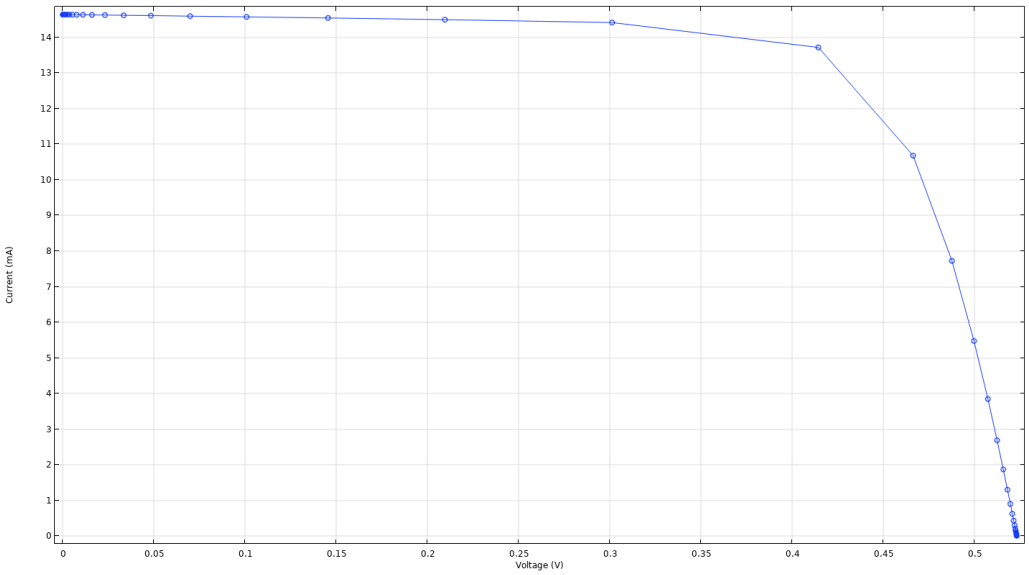

Figure 14. I-V curve of the solar cell with voltage (V) on the horizontal axis and current (mA) on the vertical axis.

To have an estimation of the generation of the solar panels for 40 min (UAV's time of flight), considering the maximum and minimum presented cases, the direct irradiance graphics were analysed in order to find the 40 min period with maximum irradiance. The "brute force" method was used, and with resource to it, it was concluded that the maximum production was from 13 h 30 min to 14 h 10 min, where both the boom's sides panels were producing energy and the irradiance incident on the wings reached its peak. Having the

wings the highest area, it was natural that its production would be more important to the results. As aforementioned, the UAV usually flies between 10 h and 16 h, so, this extreme hours were also taken into account. To calculate the total direct irradiance received by the panels over the considered times, the area of the concerning part of the graphics was determined, using a linear regression, a valid approximation due to the reduced period of time in consideration.

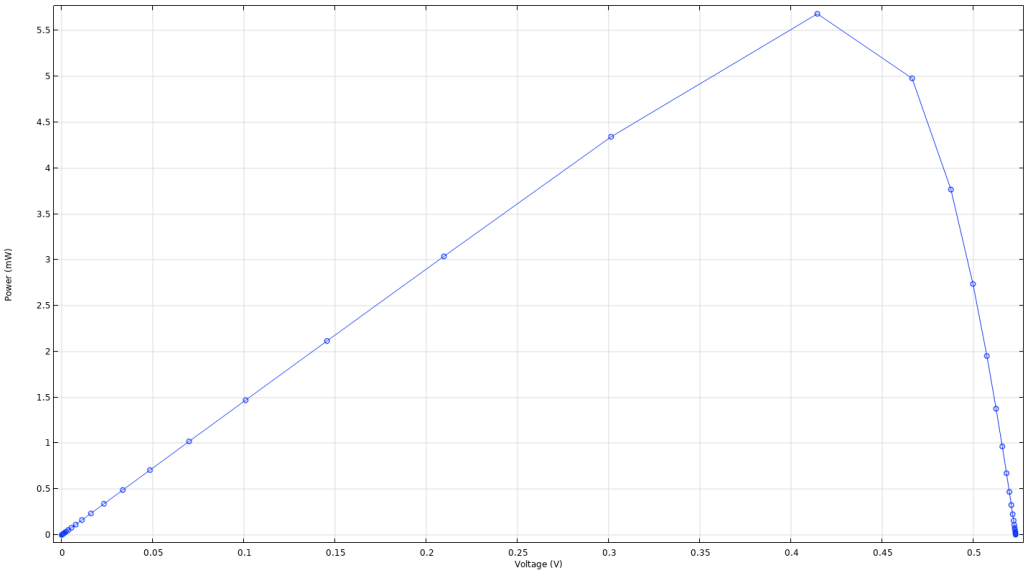

Figure 15. P-V curve of the solar cell with voltage (V) on the horizontal axis and power (mW) on the vertical axis.

With the irradiance, the efficiency and the area of the panels, the generation—the product of the three—was calculated. For the longest summer day, having the unmanned vehicle a 0° azimuth angle and −3° tilt angle, mimicking the best conditions, the produced energy for a flight at 10 am is 27.95 W h, at the maximum hour production 69.49 W h are obtained and 40 min before 16 pm is 32.98 W h. Emulating the worst conditions, the shortest winter day with the UAV flying in a 180° azimuth and the same tilt angle, the produced energy was 5.40 W h at 10 am, 21.50 W h at the maximum hour production and 9.17 W h at 15:20 pm.

As aforementioned, the unmanned vehicle uses two batteries, one for the motor and the other for the "payload". Both are Li-Po with 3.7 V of nominal voltage, being the contrast in the number of batteries. Due to the motor higher consumption, its battery is composed by 10 cells connected in series with a 10 A h capacity, while the battery for the components counts with a reduced number of 3 cells, likewise connected in series, with a 5 A h capacity. In total, the motor battery has an energy stored of 55.5 W h, while the other has 370 W h. The system UAV plus payload will need to stop either by the run out of the motor battery or the run out of the components battery, although this do not mean both the batteries will always be discharged. The consumption of energy highly depends on the payload height, mission, and type of flight, however, for the payload battery, the medium consumption is usually inferior to 2 A—which with the 5 A h capacity can last up to two and a half hours—indicating that the time of flight is shortened by the discharging of the motor battery. In this case the appropriate decision is to connect all the solar panels only to the motor battery, so that the maximum time of flight can be achieved. Knowing the motor drains up a 370 W h battery in 40 min, the calculations of the augmented time of flight with the solar panels, for each case, is simple. On the ideal summer day, the panels can give the unmanned aerial vehicle an extra time of flight between 3 min (the minimum produced at 10 am) and 7 min 30 s (the maximum energy produced by the panels). For the worst winter day, the values are much more discouraging, varying between 35 s and 2 min 19 s.

5. Conclusions

The main goal of this article was the analysis of the inclusion of solar photovoltaic panels in the augment of the UAV time of flight. Considering the surrounding parameters influence, a study was made to discard the possibility of cell fracture due to pressure resulting from air flow and altitude. After this hypothesis was eliminated, the solar panels operation, again considering the described parameters was modeled, where the interval from 35 s to 7 min 30 s was the obtained for the augmented times. While seven minutes is almost a quarter of the total time of flight, thirty five seconds is not even considered an augment. This gap of values highlights the instability of the small scale solar panels installations, which due to its reduced area, cannot always rely on the use of solar panels. Here the direction of flight is also an extra problem, as it conditions the incidence angle. Due to the sensibility to weight of the UAV, an appropriate solution would be coating the vehicle with solar paint, however that is still a technology in development. Despite this conclusion, the inclusion of the solar panels cannot be viewed as bad, for in its best case it can increase the time of flight by seven and a half minutes.

Author Contributions: J.E.C. was responsible to write the original draft, J.P.N.T. and G.C. are her supervisors, J.P.N.T. and R.A.M.L. analysed the results and they were responsible to review and editing the final manuscript. All authors have read and agreed to the published version of the manuscript.

Funding: This research received no external funding.

Institutional Review Board Statement: Not applicable.

Informed Consent Statement: Not applicable.

Data Availability Statement: Not applicable.

Acknowledgments: This work was supported in part by FCT/MCTES through national funds and in part by cofounded EU funds under Project UIDB50008/2020.

Conflicts of Interest: The authors declare no conflict of interest.

References

1. Valavanis, K.P.; Vachtsevanos, G.J. *Handbook of Unmanned Aerial Vehicles*; Springer: Dordrecht, The Netherlands, 2015.
2. Kumar, G.; Sepat, S.; Bansal, S. Review paper of solar-powered UAV. *Int. J. Sci. Eng. Res.* **2015**, *6*, 41–44.
3. Szabo, L. The history of using solar energy. In Proceedings of the 7th International Conference on Modern Power Systems (MPS'2017), Cluj-Napoca, Romania, 6–9 June 2017; pp. 1–8.
4. Durão, B.; Torres, J.P.N.; Fernandes, C.A.F.; Lameirinhas, R.A.M. Socio-economic Study to Improve the Electrical Sustainability of the North Tower of Instituto Superior Técnico. *Sustainability* **2020**, *12*, 1923. [CrossRef]
5. Melo, I.; Torres, J.P.N.; Fernandes, C.A.F.; Lameirinhas, R.A.M. Sustainability economic study of the islands of the Azores archipelago using photovoltaic panels, wind energy and storage system. *Renewables* **2020**, *7*, 1–21. [CrossRef]
6. Alves, P.; Fernandes, J.; Torres, J.; Branco, P.; Fernandes, C.; Gomes, J. Energy Efficiency of a PV/T Collector for Domestic Water Heating Installed in Sweden or in Portugal: Impact of Heat Pipe Cross-Section Geometry and Water Flowing Speed. In Proceedings of the Sdewes 2017, Dubrovnik, Croatia, 4–8 October 2017.
7. Gomes, J.; Luc, B.; Carine, G.; Fernandes, C.A.; Torres, J.P.N.; Olsson, O.; Nashih, S.K. Analysis of different C-PVT reflector geometries. In Proceedings of the 2016 IEEE International Power Electronics and Motion Control Conference (PEMC), Varna, Bulgaria, 25–30 September 2016.
8. Mota, F.; Torres, J.P.N.; Fernandes, C.A.F.; Lameirinhas, R.A.M. Influence of an aluminium concentrator corrosion on the output characteristic of a photovoltaic system. *Sci. Rep.* **2020**, *10*, 1–16. [CrossRef] [PubMed]
9. Marques, L.; Torres, J.; Branco, P. Triangular shape geometry in a Solarus AB concentrating photovoltaic-thermal collector. *Int. J. Interact. Des. Manuf. IJIDeM* **2018**, *12*, 1455–1468. [CrossRef]
10. Torres, J.P.N.; Fernandes, C.A.; Gomes, J.; Luc, B.; Carine, G.; Olsson, O.; Branco, P.J. Effect of reflector geometry in the annual received radiation of low concentration photovoltaic systems. *Energies* **2018**, *11*, 1878. [CrossRef]
11. Fernandes, C.A.; Torres, J.P.N.; Morgado, M.; Morgado, J.A. Aging of solar PV plants and mitigation of their consequences. In Proceedings of the 2016 IEEE International Power Electronics and Motion Control Conference (PEMC), Varna, Bulgaria, 25–30 September 2016.
12. Torres, J.P.N.; Nashih, S.K.; Fernandes, C.A.; Leite, J.C. The effect of shading on photovoltaic solar panels. *Energy Syst.* **2018**, *9*, 195–208. [CrossRef]

13. Fernandes, C.A.F.; Torres, J.P.N.; Branco, P.C.; Fernandes, J.; Gomes, J.R. Cell string layout in solar photovoltaic collectors. *Energy Convers. Manag.* **2017**, *149*, 997–1009. [CrossRef]
14. Fernandes, C.A.; Torres, J.P.N.; Gomes, J.; Branco, P.C.; Nashih, S.K. Stationary solar concentrating photovoltaic-thermal collector—Cell string layout. In Proceedings of the 2016 IEEE International Power Electronics and Motion Control Conference (PEMC), Varna, Bulgaria, 25–30 September 2016.
15. Campos, C.; Torres, J.; Fernandes, J. Effects of the heat transfer fluid selection on the efficiency of a hybrid concentrated photovoltaic and thermal collector. *Energies* **2019**, *12*, 1814. [CrossRef]
16. Torres, J.P.N.; Fernandes, J.F.; Fernandes, C.; Costa, B.P.J.; Barata, C.; Gomes, J. Effect of the collector geometry in the concentrating photovoltaic thermal solar cell performance. *Therm. Sci.* **2018**, *22*, 2243–2256. [CrossRef]
17. Torres, J.; Seram, V.; Fernandes, C. Influence of the Solarus AB reflector geometry and position of receiver on the output of the concentrating photovoltaic thermal collector. *Int. J. Interact. Des. Manuf. IJIDeM* **2019**, *14*, 153–172. [CrossRef]
18. Alves, P.; Fernandes, J.F.; Torres, J.P.N.; Branco, P.C.; Fernandes, C.; Gomes, J. From Sweden to Portugal: The effect of very distinct climate zones on energy efficiency of a concentrating photovoltaic/thermal system (CPV/T). *Sol. Energy* **2019**, *188*, 96–110. [CrossRef]
19. Nashih, S.K.; Fernandes, C.A.F.; Torres, J.P.N.; Gomes, J.; Costa Branco, P.J. Validation of a simulation model for analysis of shading effects on photovoltaic panels. *ASME J. Sol. Energy Eng.* **2016**, *138*, 044503. [CrossRef]
20. Blakers, A.W.; Armour, T. Flexible silicon solar cells. *Sol. Energy Mater. Sol. Cells* **2009**, *93*, 1440–1443. [CrossRef]
21. Schwingshackl, C.; Petitta, M.; Wagner, J.E.; Belluardo, G.; Moser, D.; Castelli, M.; Zebischa, M.; Tetzlaffa, A. Wind effect on PV module temperature: Analysis of different techniques for an accurate estimation. *Energy Procedia* **2013**, *40*, 77–86. [CrossRef]
22. Amajama, J. Effect of air pressure on the output of photovoltaic panel and solar illuminance (or intensity). *Int. J. Sci. Eng. Appl. Sci. IJSEAS* **2016**, *2*, 139–144.
23. Oumbe, A.; Wald, L. A parameterisation of vertical profile of solar irradiance for correcting solar fluxes for changes in terrain elevation. In Proceedings of the Earth Observation and Water Cycle Science Conference, Frascati, Italy, 18–20 November 2009; p. S05.